Strong spin-photon coupling in silicon

Samkharadze, N.; Zheng, G.; Kalhor, N.; Brousse, D.; Sammak, A.; Mendes, U. C.; Blais, A.; Scappucci, G.; Vandersypen, L. M.K.

Important note
To cite this publication, please use the final published version (if applicable).
Please check the document version above.

REPORT

QUANTUM ELECTRONICS

Strong spin-photon coupling in silicon

N. Samkharadze,[1]* G. Zheng,[1]* N. Kalhor,[1] D. Brousse,[2] A. Sammak,[2] U. C. Mendes,[3] A. Blais,[3,4] G. Scappucci,[1] L. M. K. Vandersypen[1]†

Long coherence times of single spins in silicon quantum dots make these systems highly attractive for quantum computation, but how to scale up spin qubit systems remains an open question. As a first step to address this issue, we demonstrate the strong coupling of a single electron spin and a single microwave photon. The electron spin is trapped in a silicon double quantum dot, and the microwave photon is stored in an on-chip high-impedance superconducting resonator. The electric field component of the cavity photon couples directly to the charge dipole of the electron in the double dot, and indirectly to the electron spin, through a strong local magnetic field gradient from a nearby micromagnet. Our results provide a route to realizing large networks of quantum dot–based spin qubit registers.

I n cavity quantum electrodynamics, a photon is stored in a cavity so that its interaction with a resonant atom (or other two-level system) in the cavity is enhanced to the point where a single quantum of energy is exchanged coherently between the cavity photon mode and the atom (*1*). This regime of strong coupling has been achieved across a wide range of experimental platforms, from atoms to superconducting qubits and self-assembled quantum dots, using either optical or microwave photons (*2*–*7*). Given that cavities extend over macroscopic distances, the coherent cavity-atom interaction can be used to indirectly couple well-separated atoms coherently, offering a path to scalable quantum computing.

This prospect has motivated extensive theoretical and experimental work to achieve the strong-coupling regime with gate-defined semiconductor quantum dots, one of the leading platforms for the realization of quantum circuits (*8*–*11*). Recently, strong coupling has been reported between a microwave photon and a charge qubit formed in a double quantum dot (DQD), an impressive achievement given the small electric dipole of a double dot and the short-lived charge qubit coherence (*12*–*14*). Even more chal-

lenging, but also more desirable, is the strong coupling to a spin qubit (*15*, *16*). Compared with the electron charge, the electron spin has far superior coherence properties, but its direct interaction with the cavity magnetic field is exceedingly small (*17*). Therefore, one must resort to indirect interaction of the electron spin with the cavity electric field by hybridization of the spin with the electron charge degree of freedom, without compromising spin coherence too severely in the process (*18*–*23*). For a single spin, spin-charge hybridization can be achieved in a controlled way through a transverse magnetic field gradient (*23*–*28*).

We report the observation of vacuum Rabi splitting of a single electron spin resonant with an on-chip microwave cavity, the telltale sign of strong coupling. The spin-photon coupling strength is controlled by the charge qubit settings, and we can extract all the relevant coupling strengths and decay rates. At a spin-photon coupling strength of 10 MHz, we observe cavity decay and spin dephasing rates of 4.1 and 1.8 MHz, respectively.

The superconducting cavity consists of a NbTiN half-wavelength coplanar resonator with a narrow center conductor and remote ground planes (Fig. 1, A and B), capacitively coupled to a feed line. The cavity resonator is wrapped in a square shape,

Fig. 1. Device images and schematic. (**A**) Scanning electron micrograph of a segment of the NbTiN resonator center conductor. (**B**) Optical micrograph of the resonator (square shape delineated by narrow black line) adjacent to the feed line (top) and double dot (right). The yellow square in the center is a bond pad to bias gate B. (**C**) Scanning electron micrograph showing the gates used to form the double quantum dot (DQD; white dotted circles indicate dot positions). The purple- and red-colored gates are connected to the resonator ends. White squares with X's, Fermi reservoirs connected to ohmic contacts; RP and LP, plunger gates used to control chemical potentials of the dots. (**D**) Schematic cross section of the DQD along the red dashed line in (C), showing the Si quantum well, with SiGe buffer and spacer layers, and the Al_2O_3 and SiN_x dielectrics separating the substrate from the Al gates and Co micromagnets. In the experiment, a single electron moves in the double dot potential landscape (gray line) in response to the resonator electric field E_r. A magnetic field is applied in the plane of the quantum well. The Co micromagnets create an additional magnetic field component (red curves with arrows), with a different orientation between the two dots. (**E**) The DQD energy levels as a function of DQD misalignment ε. Near $\varepsilon = 0$, the left and right dot levels hybridize, forming
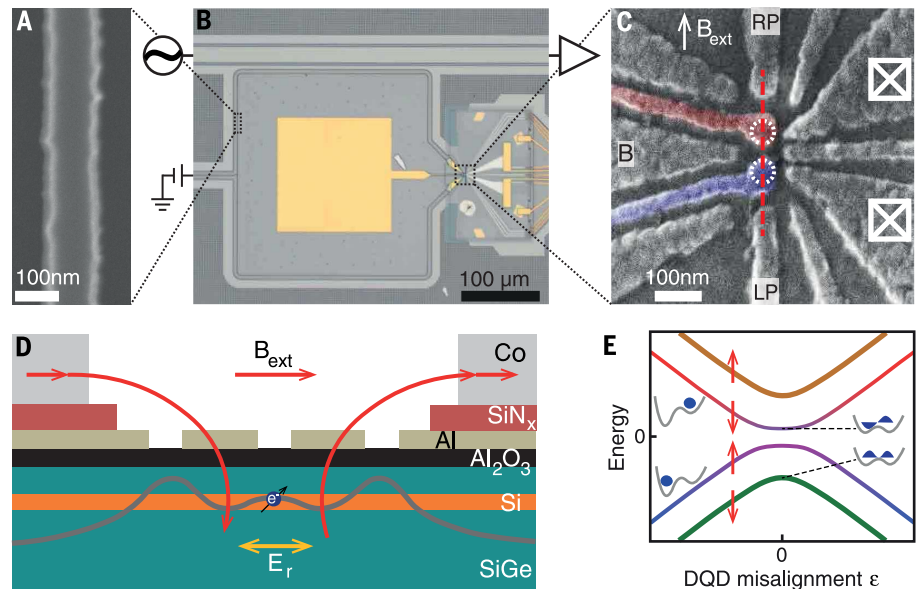
bonding and antibonding states that define a charge qubit (*34*). Each of the DQD levels is split by the Zeeman energy. The micromagnets cause spin and orbital levels to hybridize as well, as reflected in the color gradients near $\varepsilon = 0$ for the middle two energy levels.

and its two ends are connected to two Al gates that extend over the quantum dot locations. The resonator's material and dimensions give it a high characteristic impedance of about 1 kilohm that enhances the coupling g_c to the double dot charge dipole (13, 29) and make it resilient to in-plane magnetic fields of up to 6 T (29). The DQD is formed electrostatically in an undoped Si/SiGe quantum well (natural isotopic abundance), using a single layer of Al gates (30) (Fig. 1C). A positive bias on a gate accumulates electrons in the quantum well underneath, and a negative bias repels electrons (fig. S1D). An external in-plane magnetic field B_{ext} induces a Zeeman splitting on an electron in the DQD. Two cobalt micromagnets placed near the quantum dots (fig. S1, B and C) produce an additional local in-plane magnetic field, as well as a transverse magnetic field gradient. As a result, when an electron oscillates between the two dots, it experiences an oscillating transverse magnetic field, providing the necessary (indirect) spin-charge hybridization that allows an electric field to couple to the spin (24–26) (Fig. 1E).

We apply a probe tone to the feed line at frequency f_p and record the transmission through the feed line (unless indicated, all transmission plots show the normalized amplitude of the transmission through the feed line). With the DQD tuned to keep the electron fixed in one of the dots, the transmission shows a dip for f_p near 6.051 GHz, the bare resonance frequency f_r of the NbTiN resonator (Fig. 2B, square symbol). From the linewidth, we find the bare resonator decay rate $\kappa_r/2\pi = 2.7$ MHz, with an internal loss rate $\kappa_{int}/2\pi = 1.5$ MHz (fig. S5). We monitor the transmission through the feed line at low probe power (below –125 dBm, corresponding to <1 photon in the resonator) to tune up the DQD, characterize the charge-photon interaction, and study spin-photon coupling.

To characterize the charge-photon interaction, we tune the DQD to a regime where the electron can move back and forth between the two dots in response to the cavity electric field, setting $B_{ext} = 110$ mT, well above the spin-photon resonance condition. Such motion is possible whenever the electrochemical potentials of the two dots are aligned—i.e., where it costs equal energy for an electron to be in either dot. This occurs for specific combinations of gate voltages, seen as the short bright lines in Fig. 2A, where the charge-photon interaction modifies the transmission (31). We focus on the lower left line, which corresponds to the last electron in the DQD.

To place the charge-photon interaction in the dispersive regime, the gate voltages are adjusted to set $2t_c/h$ in the range of 8 to 15 GHz, so that the charge qubit splitting $hf_c = \sqrt{4t_c^2 + \varepsilon^2}$ is always well above hf_r (t_c, interdot tunnel coupling; h, Planck's constant). We measure f_c using two-tone spectroscopy. In the dispersive regime, the charge-photon interaction results in a frequency shift of the resonator (Fig. 2F). In Fig. 2B, the characteristic dependence of this dispersive shift on the DQD misalignment ε is apparent. At $\varepsilon = 0$, the electron can most easily move between the dots; hence, the electrical susceptibility is the highest, and the dispersive shift the largest (triangle). At $\varepsilon = 0$, the magnitude of the dispersive shift is approximated by $(g_c/2\pi)^2/(f_c - f_r)$, where the charge-photon coupling strength g_c is mostly fixed by design, and the detuning between f_c and f_r can be adjusted. From a fit based on input-output theory (32), a charge-photon coupling strength $g_c/2\pi$ of ~200 MHz is extracted.

To probe coherent spin-photon coupling, the charge sector parameters are kept constant so that the interaction with charge remains dispersive.
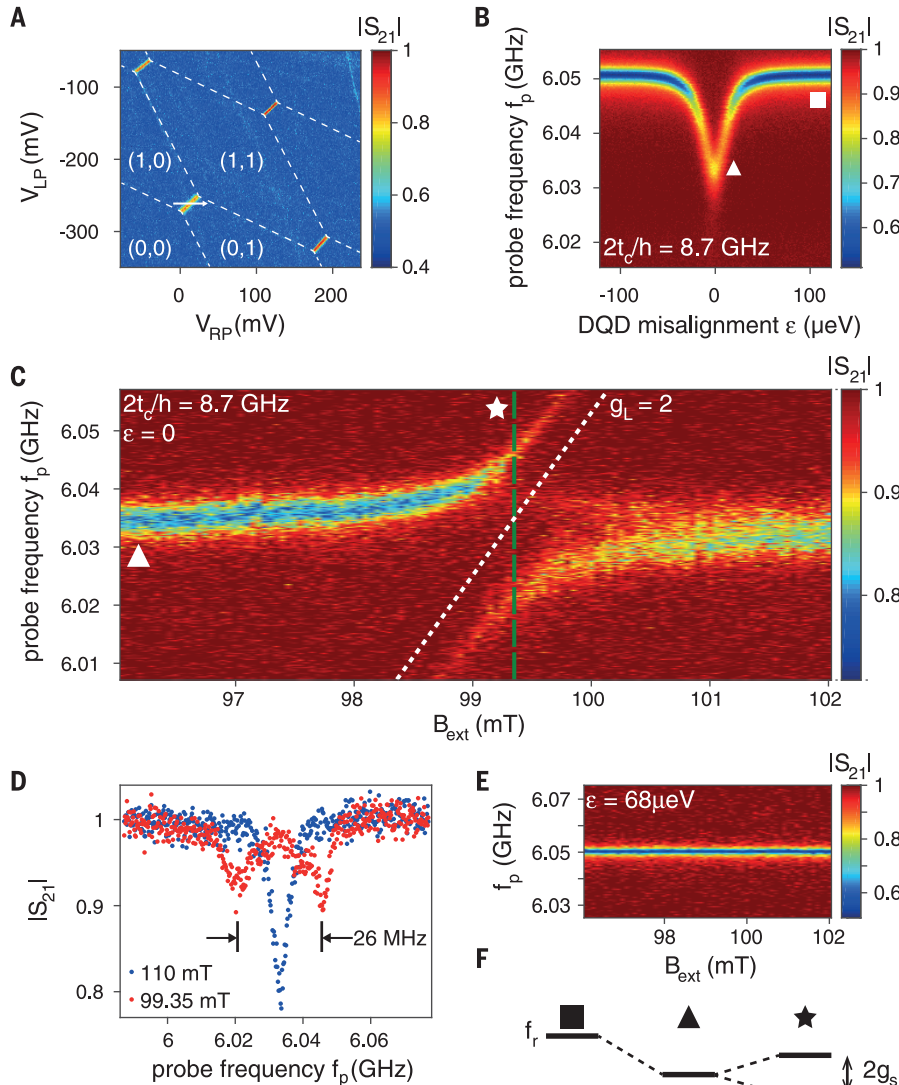

Fig. 2. Strong spin-photon coupling. (**A**) Normalized amplitude S_{21} of the transmission through the feed line, probed at $f_p = 6.051$ GHz. At the four short bright lines, the electron can move between the dots. The dashed lines connecting the short lines indicate alignment of a dot with a reservoir electrochemical potential. Labels indicate the electron number in the two dots. The DQD misalignment ε is varied along the direction of the white arrow, causing an inconsequential uniform shift in the DQD potential as well. (**B**) Transmission as a function of ε and f_p. At large $|\varepsilon|$, we measure the bare resonator transmission (square). Near $\varepsilon = 0$, the DQD charge qubit interacts dispersively with the cavity frequency, leading to a characteristic frequency shift (triangle). (**C**) Transmission as a function of B_{ext} and f_p. When B_{ext} makes the spin splitting resonant with the resonator frequency (star), a clear avoided crossing occurs, which we attribute to the strong coupling of a single spin and a single photon. The white dotted line shows the expected spin splitting for a spin in silicon. (**D**) Line cut through (C) at the position of the green dashed vertical line (red data points) and line cut at 110 mT (blue points). The red data show clear vacuum Rabi splitting. (**E**) Similar to (C), but with the DQD misaligned, so the electron cannot move between the two dots. The spin-photon coupling is no longer visible. (**F**) Schematic representation of the transmission resonance of the superconducting cavity. The bare transmission resonance (square) is shifted dispersively by its interaction with the charge qubit (triangle) and splits when it is resonant with the spin qubit (star).

By varying B_{ext}, the spin splitting is controlled so that the interaction with the spin goes from dispersive to resonant. On resonance, spin and photon hybridize (Fig. 2F, star). In Fig. 2C, the transmission through the feed line is shown as a function of the strength of B_{ext} (the total field is the vector sum of the external field and the micromagnet stray field) and the probe frequency f_p applied to the feed line. As expected, the cavity resonance seen in transmission is (nearly) independent of B_{ext} at large spin-resonator detuning. When the spin splitting approaches resonance with the resonator frequency, we observe a strong response in the form of an anticrossing (Fig. 2C, star). The slope f_p/B_{ext} of the slanted

Fig. 3. Two-tone spectroscopy of the charge and spin qubit. (**A**) Transmission at $f_p = 6.041$ GHz as a function of DQD misalignment ε and the frequency f_s of a second tone (pump frequency) that is applied to gate LP. When the second tone
is in resonance with the charge qubit splitting (white dashed line), the steady-state
occupation of the charge qubit is changed, and, owing to the charge-photon coupling, this is reflected in a modified dispersive shift of the resonator. (**B**) Line cut at $\varepsilon = 0$, from which we extract a charge qubit dephasing rate of 52 MHz. (**C**) Transmission (phase response) at $f_p = 6.043$ GHz as a function of B_{ext} and the pump frequency applied to gate LP. When the pump frequency is in resonance with the spin qubit splitting, the steady-state occupation of the spin qubit is changed, and, owing to the spin-photon coupling, this is reflected in a modified response of the resonator. The slope of the response corresponds to a spin with $g_L \approx 2$. (**D**) Line cut at $B_{ext} = 100.1$ mT, from which we extract a spin qubit dephasing rate of 1.4 MHz.
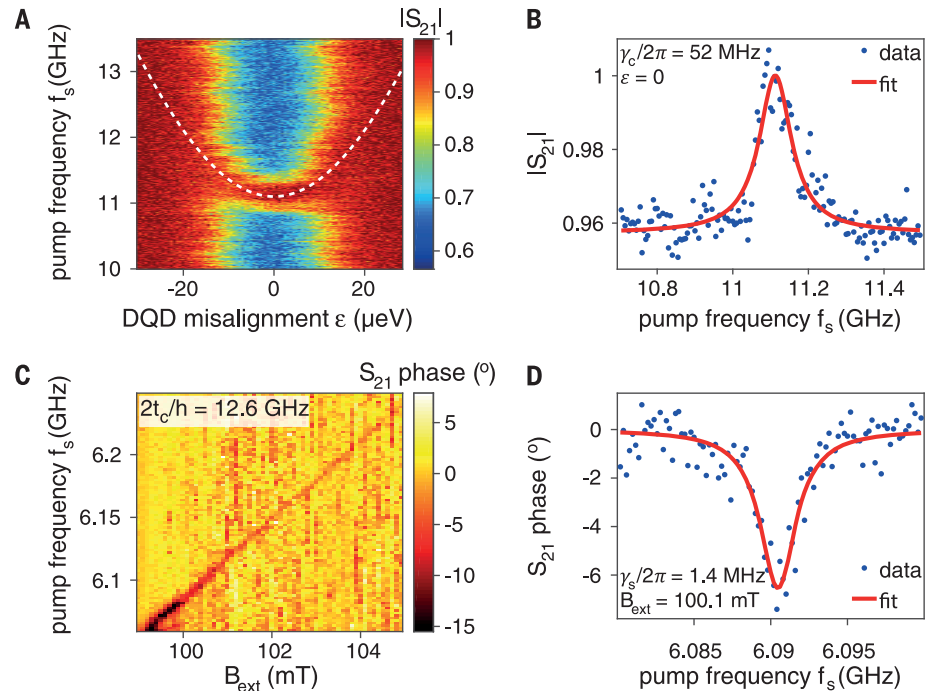
Fig. 4. Control of the spin-photon coupling. (**A**) The dependence on DQD tunnel coupling of g_s, κ, and γ_s (upper panel) and of the ratio of peak splitting to linewidth $2g_s/(\gamma_s + \kappa/2)$ (lower panel) for $\varepsilon = 0$. Although all three separate quantities increase with lower t_c, the ratio $2g_s/(\gamma_s + \kappa/2)$, which is the most relevant quantity, shows an optimum value around $f_c = 9.5$ GHz. The black dashed line shows g_s approximated as $\frac{1}{4}g_c g_L \mu_B \Delta B_x/(2t_c/h - f_r)$ (28), taking ΔB_x = 20 mT (which translates to an estimated interdot distance of 45 nm, given the 0.45 mT/nm simulated transverse gradient). (**B** to **D**) Similar data to
Fig. 2C for three different values of DQD tunnel coupling, as indicated. The small differences in the resonant magnetic
field are mostly due to different magnetic field sweep histories and hysteresis in
the micromagnet. (**E**) Transmission as a function of B_{ext} and ε for $2t_c/h = 10.3$ GHz and $f_p = 6.040$ GHz. Where the blue band
is interrupted, the Zeeman splitting is resonant with the (dispersively shifted) resonator.
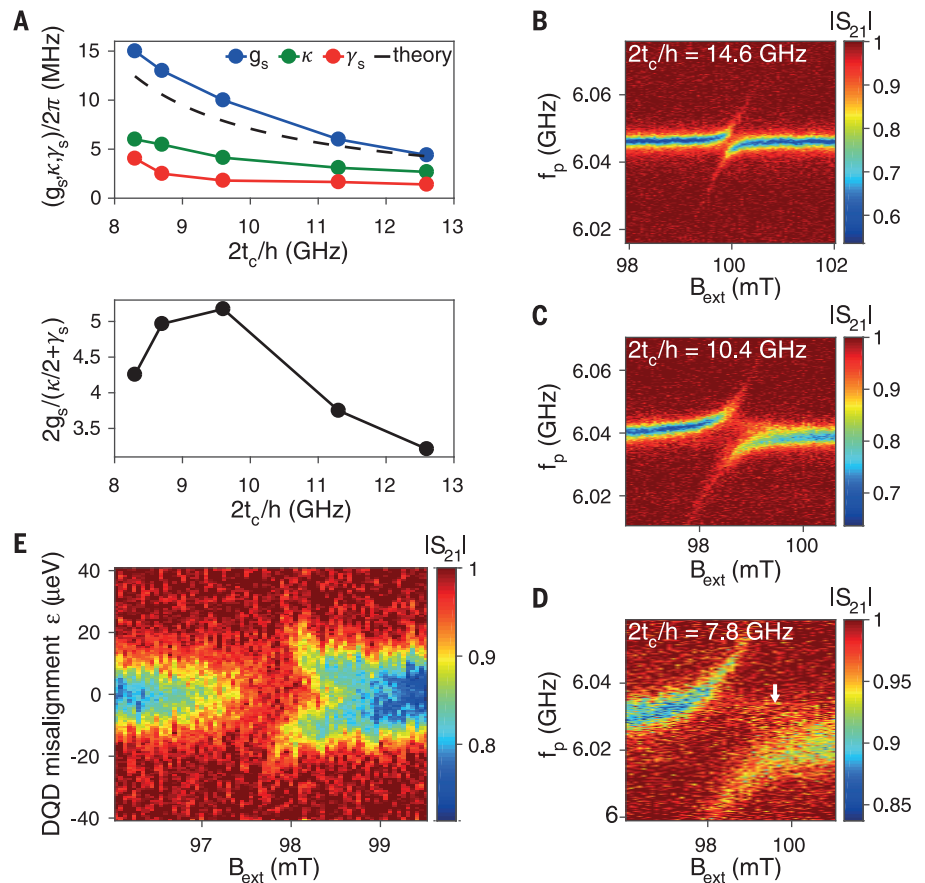
branch corresponds to $g_L \mu_B/h$ (μ_B, the Bohr magneton; $g_L \approx 2$, the Landé g-factor of an electron spin in Si). The observed avoided crossing is thus a clear signature of the coherent hybridization of the spin qubit with a single microwave photon.

The line cut indicated by the dashed green line in Fig. 2C and shown in Fig. 2D reveals two well-separated peaks. This feature is known as the vacuum Rabi splitting and is expected for strong coherent spin-photon coupling. The peak separation is about 26 MHz, corresponding to a spin-photon coupling strength $g_s/2\pi$ of 13 MHz. The cavity decay rate can be extracted independently from the linewidth away from spin-photon resonance, which here is $\kappa/2\pi = 5.4$ MHz [the cavity dispersively interacts with the charge, so $\kappa > \kappa_r$ (31)]. The spin dephasing rate $\gamma_s/2\pi = 2.5$ MHz is independently obtained from two-tone spectroscopy of the spin transition (discussed next). We observe that $g_s > \kappa, \gamma_s$, satisfying the condition for strong coupling of a single electron spin to a single microwave photon.

Two-tone spectroscopy of the charge and spin qubits allows us to independently extract the respective qubit splittings and dephasing rates. In Fig. 3, A and B, the second tone is resonant with the charge qubit splitting around 11.1 GHz, with a dependence on ε described by $hf_c = \sqrt{4t_c^2 + \varepsilon^2}$ [white dashed line (neglecting spin-charge hybridization)]. In this case, a charge qubit dephasing rate $\gamma_c/2\pi = 52$ MHz is extracted from the linewidth. In Fig. 3, C and D, the second tone is swept through the spin resonance condition while keeping the spin-cavity system in the dispersive regime. A linear dependence of the spin splitting on B_{ext} is observed, with a slope corresponding to $g_L \approx 2$. At $2t_c/h = 12.6$ GHz, we extract $\gamma_s/2\pi = 1.4$ MHz from the linewidth. This is somewhat larger than the ~0.3-MHz single-spin dephasing rates observed in a single Si/SiGe quantum dot (10, 11, 25), as is expected given that an electron in a DQD at $\varepsilon = 0$ is more susceptible to charge noise, which affects spin coherence through the magnetic field gradient (23, 27, 28).

The spin-photon hybridization can be controlled with gate voltages. By moving away from $\varepsilon = 0$, the photon and charge no longer hybridize, and the spin-photon coupling vanishes (Fig. 2E). Furthermore, at $\varepsilon = 0$, the spin-photon coupling strength can be approximated as $g_s = \frac{1}{4} g_c g_L \mu_B \Delta B_x/(2t_c/h - f_r)$ (provided the magnetic field profile is symmetric relative to the DQD) (23, 27, 28). Here, ΔB_x is the difference in the transverse field between the two dots. Starting from large t_c, reducing t_c increases spin-charge admixing—and thus, indirectly, spin-photon coupling—as seen experimentally in Fig. 4, B to D. With increased spin-charge admixing, the asymmetry in the intensity of the two branches also increases, which is understood as a result of quantum interference in the one-excitation manifold of pho-

ton, charge, and spin (28). Furthermore, an additional feature (Fig. 4D, white arrow) appears close to the lower branch (discussed in the supplementary materials). The variation of g_s with t_c is summarized in Fig. 4A, along with the theoretical approximation for g_s versus t_c. However, as seen in the same figure, with lower t_c, the spin dephasing rate γ_s increases as well, as does the cavity decay rate κ (28). Ultimately, we wish to maximize the peak separation over linewidth, $2g_s/(\gamma_s + \kappa/2)$. In this respect, there is an optimal choice of tunnel coupling, as seen from Fig. 4A.

Last, we study how close together the charge and spin sweet spots occur, where the relevant frequency (charge or spin) is, to first order, insensitive to the DQD misalignment. The charge sweet spot is seen in Fig. 2B at $\varepsilon = 0$ and $f_p = 6.032$ GHz. If the micromagnets are placed symmetrically with respect to the DQD (as in Fig. 1D), the total magnetic field magnitude is symmetric around the center of the DQD. In this case, the spin splitting has no first-order dependence on ε at $\varepsilon = 0$, and the charge and spin sweet spots coincide. For asymmetrically placed magnets, the spin sweet spot occurs away from $\varepsilon = 0$. To find the spin sweet spot, we vary ε and B_{ext} at $f_p = 6.040$ GHz (Fig. 4E). Throughout the blue band, f_p is resonant with the cavity frequency (in the dispersive charge-photon coupling regime). Where the blue band is interrupted, the magnetic field brings the spin on resonance with the cavity photon, spin and photon hybridize, and the transmission is modified. This spin-photon resonance condition shifts down in magnetic field as a function of $|\varepsilon|$ (26). The value of ε where this shift has no first-order dependence on ε occurs close to $\varepsilon = 0$, i.e., the spin sweet spot lies close to the charge sweet spot.

The strong coupling of spin and photon not only opens a new range of physics experiments, but also is the crucial requirement for coupling spin qubits at a distance by means of a superconducting resonator. Given the large dimensions of resonators compared with those of double dots, multiple spin qubits can interact with and through the same resonator, enabling scalable networks of interconnected spin qubit registers (33). Importantly, the spin-photon coupling can be switched on or off on nanosecond time scales by using gate voltage pulses that control the double dot misalignment and tunnel coupling, facilitating on-demand coupling of one or more spins to a common resonator.

REFERENCES AND NOTES

1. S. Haroche, J.-M. Raimond, *Exploring the Quantum: Atoms, Cavities, and Photons* (Oxford Univ. Press, 2006).
2. R. J. Thompson, G. Rempe, H. J. Kimble, *Phys. Rev. Lett.* **68**, 1132–1135 (1992).
3. M. Brune et al., *Phys. Rev. Lett.* **76**, 1800–1803 (1996).
4. A. Wallraff et al., *Nature* **431**, 162–167 (2004).
5. I. Chiorescu et al., *Nature* **431**, 159–162 (2004).
6. J. P. Reithmaier et al., *Nature* **432**, 197–200 (2004).
7. T. Yoshie et al., *Nature* **432**, 200–203 (2004).
8. M. D. Shulman et al., *Science* **336**, 202–205 (2012).
9. M. Veldhorst et al., *Nature* **526**, 410–414 (2015).
10. T. F. Watson, S. G. J. Philips, E. Kawakami, D. R. Ward, P. Scarlino, M. Veldhorst, D. E. Savage, M. G. Lagally, M. Friesen, S. N. Coppersmith, M. A. Eriksson, L. M. K. Vandersypen, arXiv:1708.04214 [cond-mat.mes-hall] (14 August 2017).
11. D. M. Zajac et al., *Science* **359**, 439–442 (2018).
12. X. Mi, J. V. Cady, D. M. Zajac, P. W. Deelman, J. R. Petta, *Science* **355**, 156–158 (2017).
13. A. Stockklauser et al., *Phys. Rev. X* **7**, 011030 (2017).
14. L. E. Bruhat, T. Cubaynes, J. J. Viennot, M. C. Dartiailh, M. M. Desjardins, A. Cottet, T. Kontos, arXiv:1612.05214 [cond-mat.mes-hall] (15 December 2016).
15. X. Mi, M. Benito, S. Putz, D. M. Zajac, J. M. Taylor, G. Burkard, J. R. Petta, arXiv:1710.03265 [cond-mat.mes-hall] (9 October 2017).
16. A. J. Landig, J. V. Koski, P. Scarlino, U. C. Mendes, A. Blais, C. Reichl, W. Wegscheider, A. Wallraff, K. Ensslin, T. Ihn, arXiv:1711.01932 [cond-mat.mes-hall] (6 November 2017).
17. P. Haikka, Y. Kubo, A. Bienfait, P. Bertet, K. Mølmer, *Phys. Rev. A* **95**, 022306 (2017).
18. L. Childress, A. S. Sørensen, M. D. Lukin, *Phys. Rev. A* **69**, 042302 (2004).
19. G. Burkard, A. Imamoglu, *Phys. Rev. B* **74**, 041307 (2006).
20. M. Trif, V. N. Golovach, D. Loss, *Phys. Rev. B* **77**, 045434 (2008).
21. A. Cottet, T. Kontos, *Phys. Rev. Lett.* **105**, 160502 (2010).
22. C. Kloeffel, M. Trif, P. Stano, D. Loss, *Phys. Rev. B* **88**, 241405 (2013).
23. F. Beaudoin, D. Lachance-Quirion, W. A. Coish, M. Pioro-Ladrière, *Nanotechnology* **27**, 464003 (2016).
24. M. Pioro-Ladrière, Y. Tokura, T. Obata, T. Kubo, S. Tarucha, *Appl. Phys. Lett.* **90**, 024105 (2007).
25. E. Kawakami et al., *Nat. Nanotechnol.* **9**, 666–670 (2014).
26. J. J. Viennot, M. C. Dartiailh, A. Cottet, T. Kontos, *Science* **349**, 408–411 (2015).
27. X. Hu, Y.-X. Liu, F. Nori, *Phys. Rev. B* **86**, 035314 (2012).
28. M. Benito, X. Mi, J. M. Taylor, J. R. Petta, G. Burkard, *Phys. Rev. B* **96**, 235434 (2017).
29. N. Samkharadze et al., *Phys. Rev. Appl.* **5**, 044004 (2016).
30. S. Rochette, M. Rudolph, A.-M. Roy, M. Curry, G. Ten Eyck, R. Manginell, J. Wendt, T. Pluym, S. M. Carr, D. Ward, M. P. Lilly, M. S. Carroll, M. Pioro-Ladriare, arXiv:1707.03895 [cond-mat.mes-hall] (12 July 2017).
31. T. Frey et al., *Phys. Rev. Lett.* **108**, 046807 (2012).
32. K. D. Petersson et al., *Nature* **490**, 380–383 (2012).
33. L. M. K. Vandersypen et al., *npj Quantum Inf.* **3**, 34 (2017).
34. T. Hayashi, T. Fujisawa, H. D. Cheong, Y. H. Jeong, Y. Hirayama, *Phys. Rev. Lett.* **91**, 226804 (2003).

SUPPLEMENTARY MATERIALS

www.sciencemag.org/content/359/6380/1123/suppl/DC1
Materials and Methods
Supplementary Text
Figs. S1 to S5

Science

Strong spin-photon coupling in silicon

N. Samkharadze, G. Zheng, N. Kalhor, D. Brousse, A. Sammak, U. C. Mendes, A. Blais, G. Scappucci and L. M. K. Vandersypen

Coupling light to single spins

To help develop quantum circuits, much effort has been directed toward achieving the strong-coupling regime by using gate-defined semiconductor quantum dots. Potentially, the magnetic dipole, or spin, of a single electron for use as a qubit has advantages over charge-photon coupling owing to its longer lifetime. Samkharadze *et al.* hybridized the electron spin with the electron charge in a double silicon quantum dot. This approach yielded strong coupling between the single electron spin and a single microwave photon, providing a route to scalable quantum circuits with spin qubits.

Science, this issue p. 1123

ARTICLE TOOLS	http://science.sciencemag.org/content/359/6380/1123
SUPPLEMENTARY MATERIALS	http://science.sciencemag.org/content/suppl/2018/01/24/science.aar4054.DC1
REFERENCES	This article cites 29 articles, 4 of which you can access for free http://science.sciencemag.org/content/359/6380/1123#BIBL
PERMISSIONS	http://www.sciencemag.org/help/reprints-and-permissions

Use of this article is subject to the Terms of Service